Section 2

Data sets, diagnostic and dynamical investigations, statistical post-processing, reanalysis, and associated studies.

TRENDS OF WIND SPEED IN LOW TROPOSPHERE FROM GLOBAL RADIOSONDE DATA

O. A. Aldukhov and I. V. Chernykh
Russian Institute of Hydrometeorological Information – World Data Center, Obninsk, Russia, E-mail: aoa@meteo.ru, civ@meteo.ru

Introduction

The knowledge about long-term changes in wind speed (S) distribution in the low troposphere is necessary for studies of global climate change, geo-economic justification of nuclear power stations construction, needs of aviation, shipping and other science and practical needs. The paper presents the trends in the time series of wind speed in the low tropospheric layer from the surface to the 2-km height over the Globe for different months, seasons, and a year. In addition, the estimates of the trend long-term changes are presented in dependence of the trend computing period.

Data and methods

The computations are based on the radiosonde data of 683 stations from the global aerological network. Data from aerological dataset CARDS [1] supplemented by current data from datasets AROCTAB [2] and AROCTAC [3] for the observational period of 1964—2018 were used for this research. The data were subject to a complex quality control procedure.

The Akima cubic spline interpolation method was used for calculating S in the tropospheric layer 0—2 km over the surface level with taking into account specific points of the vertical profiles. The necessary condition for including a station from the global aerological network to research for the full period of 1964—2018 was the presence of observations for 1990—2010. The trends for every station were estimated using the least squares method. The anomalies were calculated with respect to the corresponding long-term mean values S for the full period of 1964—2018. The trend long-term changes were estimated using the corresponding time series of the trends calculated by reducing periods with approaching to the end of 2018. The values obtained for each station were averaged for the Globe taking into account the square of the station influencing area.

Results

Figs. (a—c) show that the spatiotemporal distributions of the long-term means S, their trends, and the tendency of the trend changes are not uniform in the layer 0—2 km above the surface. The range of inter-annual changes of the linear trends of anomalies of the long-term monthly means S in the 0—2-km low tropospheric layer is of -0,075—0,274 m/s *decade^{-1} (Fig. b). The wind speed in this layer over the Globe increases mainly at 0,4—0,7 km above the surface. We can see negative trends near the surface.

The tendency of the trends increase (Fig. c) is detected mainly at 1—2 km above the surface from November to July and also at the heights of 0,1—0,4 km — from May to July. The trend long-term changes vary from 0,020 to 0,113 m/s *decade^{-2} for different months.

Conclusions

The spatiotemporal distributions of the trends and the linear trends of the wind speed trends are not uniform in the tropospheric layer 0—2 km over the Globe. The wind speed increases mainly at the heights of 0,4—0,7 km. The tendency of the trends increasing can be seen at the heights of 1—2 km for most of the year.

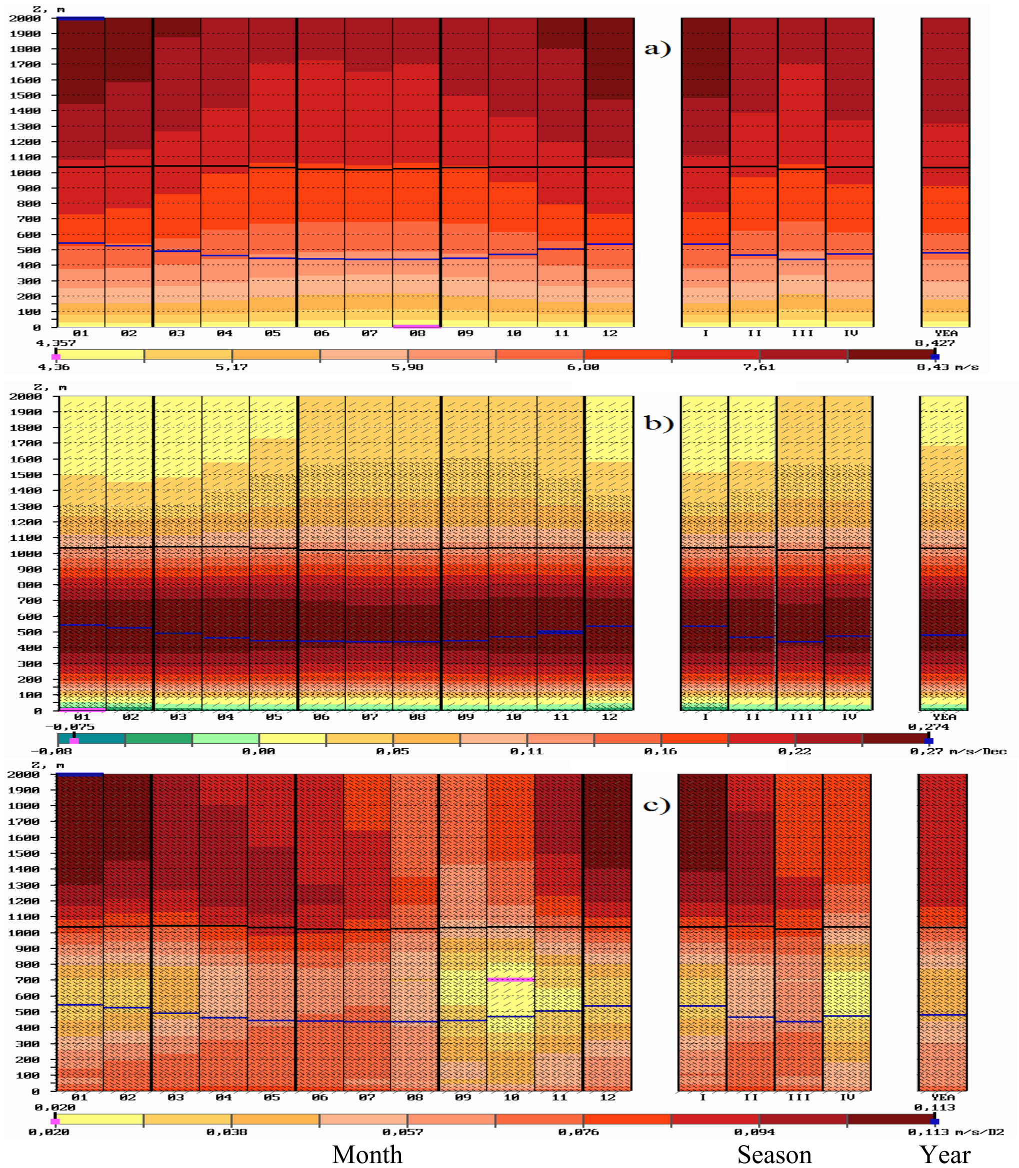

Fig. Long-term mean values (a) for wind speed, m/s; the linear trends of anomalies of long-term means (b) for wind speed, m/s *decade^{-1}; the linear trends of the wind speed trends (c), m/s *decade^{-2}, in the low tropospheric layer 0—2 km for every month, season (I, II, III, IV for DJF, MAM, JJA, SON correspondingly), and for a year. The global statistics for months and seasons were subject to a twofold smoothing. The three–points smoothing was used. Trends with significance not less than 50% are marked by sloping line segments and with significance not less than 95% — by lattice. Blue and pink segments correspond to maximum and minimum values. Black and blue lines correspond to heights of mixing level and surface inversion in 1964—2018.

References

1. Eskridge R.E., Alduchov O.A., Chernykh I.V., Zhai P., Polansky A.C., Doty S.R. A comprehensive aerological reference dataset (CARDS): rough and systematic errors // Bull. Amer. Meteor. Soc. 1995. **76.** 1759-1775.
2. Aldukhov O.A. et al. Dataset of current aerological information AROCTAB. Description of the dataset. – Obninsk, RIHMI-WDC, 1990, 28 p.
3. Rudenkova T.V. Format for archiving of the current aerological data, received from GTS for PC // Proc. RIHMI-WDC, 2010, N 174, p. 41—63.

Estimates of Cloud Layers Number from Global Atmospheric Radiosounding Data

I.V. Chernykh and O.A. Aldukhov

Russian Institute of Hydrometeorological Information – World Data Center, Obninsk, Russia,
E-mail: civ@meteo.ru, aoa@meteo.ru

The number of cloud layers is one of the main parameters of cloudiness vertical macrostructure [1]. In this study, the number of cloud layers with cloud amounts of 0–20, 20–60, 60–80, 80–100, 0–100% of the sky covered are estimated for the Globe. Calculations were conducted for the atmospheric layer 0–10 km above the surface level and annual means were found.

In this research we used the CE-method for cloud boundaries and cloud amount reconstruction [2, 3] and radiosonde sounding data for 965 aerological stations from global dataset CARDS [4] supplemented by current data from datasets AROCTAB [5] and AROCTAC [6] for the 1964-2017 period. To compute the statistics for the stations, only observations including both temperature and humidity data from the surface to the height of 10 km were applied. The existence of several cloud layers with different cloud amounts was allowed. We did not consider cloud layers for which the CE-method gave thickness less than 50 m. We used the weighted anisotropic interpolation method for interpolating the statistical characteristic to 2°×2° grid.

The global annual mean cloud layer numbers for different cloud amount gradations and their standard deviations are presented in the Table for atmospheric layer of 0–10 km over the surface level. The second and the third columns show globally averaged values while the regional ranges of variations of the cloud layer numbers are presented in columns four and five. The geographic distribution of the annual mean numbers of cloud layers with 0–100% cloud amounts and their standard deviations are shown in Figure for the atmospheric layer considered in the study.

Table.

The global annual mean cloud layer numbers and their standard deviations with taking into account the cloud amount gradation and their regional variations ranges for atmospheric layer of 0–10 km over the surface level. 1964–2017. See text for details.

The cloud amount gradation, % of the sky surface	Mean	σ	Mean	σ	Number of observations, thousands
0–20	4,2	2,5	1,7–7,3	0,8–4,2	1,2–36,3
20–60	1,5	0,8	1,1–2,0	0,4–1,2	0,5–21,6
60–80	1,2	0,4	1,0–1,4	0,2–0,6	0,3–13,1
80–100	2,6	1,8	1,4–4,5	0,7–3,5	0,7–31,6
0–100	6,5	3,1	2,2–10,5	1,0–5,4	1,5–37,9

The presented results demonstrate that the mean cloud layer numbers and their standard deviations depend on the cloud amount gradation, 0–20, 20–60, 60–80, 80–100% of the sky surface. Their values for the gradations 0–20 and 80–100% are several times higher than for the gradations 20–60, 60–80%. The geographic distributions of the annual mean numbers of cloud layers with 0–100% cloud amounts and their standard deviations for atmospheric layer 0–10 km are uniform enough over most part of the Globe. The minimum is detected over Tibet while the maximum is found near the southern point of South America.

a)

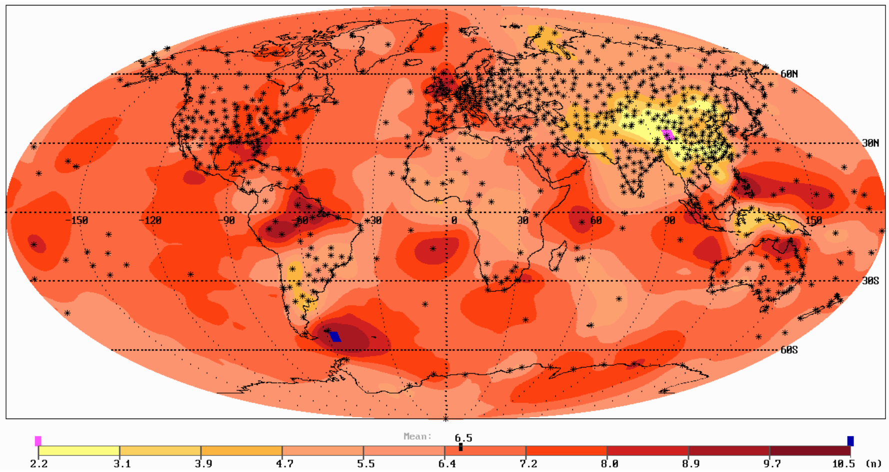

b)

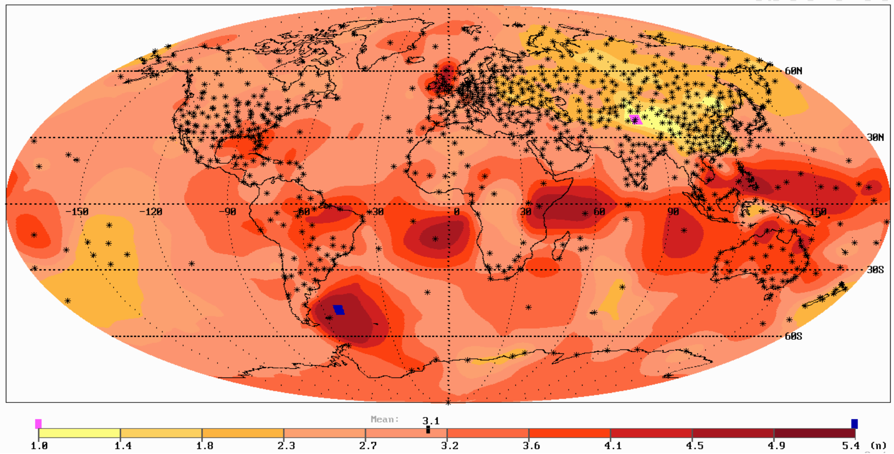

*The geographic distribution of the annual mean numbers of cloud layers with 0–100% cloud amounts (a) and their standard deviations (b) for the atmospheric layer of 0–10 km over the surface. * – 965 stations. 1964–2017.*

Long-term estimations of cloud layer number may be useful for studying the atmospheric radiation energy, for assessing propagation conditions of electromagnetic waves, for supporting the aviation operation, for interpretation of cloud parameters determined by other methods.

References

1. Chernykh I.V., Aldukhov O.A. Estimating the number of cloud layers through radiosonde data from Russian aerological station for 1964-2014 // Russian Meteorology and Hydrology, 2018, Vol. 43, No. 3, pp. 152–160.
2. Chernykh I.V. and Eskridge R.E. Determination of cloud amount and level from radiosonde soundings // J. Appl. Meteorol., 1996, vol. 35, pp. 1362—1369.
3. Chernykh I.V., Aldukhov O.A. Vertical distribution of cloud layers from cloud radiosounding data // Izvestiya, Atmospheric and Oceanic Physics. 2004. **40.** No 1. 41-53.
4. Eskridge R.E., Alduchov O.A., Chernykh I.V., Zhai P., Polansky A.C., Doty S.R. A comprehensive aerological reference dataset (CARDS): rough and systematic errors // Bull. Amer. Meteor. Soc. 1995. **76.** 1759-1775.
5. Aldukhov O.A. et al. Dataset of current aerological information AROCTAB. Description of the dataset. – Obninsk, RIHMI-WDC, 1990, 28 p.
6. Rudenkova T.V. Format for archiving of the current aerological data, received from GTS for PC // Proc. RIHMI-WDC, 2010, N 174, p. 41—63.

Pre-operational runs of atmospheric model COSMO-Ru with initial snow data from 1D multilayer snow model SnoWE

E. Churiulin (1, 2), V.Kopeykin(1), I. Rozinkina (1, 2)
Contact: evgenychur@gmail.com
(1) Hydrometcenter of Russia, Bolshoy Predtechensky per., 123242, Moscow, Russia
(2) Faculty of Geography, Lomonosov Moscow State University, GSP-1, Leninskie Gory, 119991, Moscow, Russia

The investigation is devoted to the development of new runoff forecast methods in modern climate conditions on the example of floods on the Sukhona river near Velikiy Ustyug. The main purpose of the research is creation of a new scheme of assimilation and application of observations (in situ) and model data (COSMO-Ru [1] and SnoWE [3]) for a hydrological model ECOMAG (the model of runoff formation - author Motovilov Yu.G., Institute of Water Problem of RAS [2]). For analysis of flood characteristics, the most promising method is synthesizing models of the hydrometeorological cycle.

The initial and boundary data for the mesoscale COSMO-Ru system are taken from the global ICON model [5]. The comparisons of ICON snow water equivalent (SWE) values with the results of the hydrological model and in situ measurements demonstrated some serious inaccuracies for the territory of the Russian Federation with a permanent snow cover (Fig.1).

Initial meteorological data for the hydrological model ECOMAG were obtained from in-situ observations and (or) the mesoscale atmospheric circulation model COSMO-Ru. Thus, we had to launch the hydrological model on the COSMO-Ru grids. The information about snow and snow cover characteristics was obtained from the SnoWE with different spatial steps.

The SnoWE program complex is based on the 1-d multilayer model of snow evaluation for synoptic meteorological stations based on synoptic measurements. The 1-d multilayer model calculates daily values of SWE and changes in snow density (SD). In the SnoWE program complex, two different schemes of modelling SWE and SD values are implemented.

The focus of this research is coupling the hydrological (ECOMAG) and meteorological (COSMO-Ru) models and linking ECOMAG and the snow model. The second purpose is the comparison of snow cover from ECOMAG and SnoWE for the research territory.

The research was done for two time periods from 01.09.2017 to 01.06.2018 and from 01.09.2018 to the present based on the COSMO-Ru system with different spatial resolutions (COSMO-Ru13 – 13 km: all territory of Russia and neighboring areas; COSMO-Ru7 – 7 km: European part of Russia and the nearest areas, COSMO-Ru2 – 2.2 km: Central Russian regions) in quasi-operational mode. The results demonstrated that the fields of snow cover from SnoWE (with ICON data as the first guess fields) contain less errors and are a positive alternative to ICON data.

This approach can be effective for analyzing possible extreme hydrometeorological events and allows to solve diverse problems associated with the flooding of the territory, both in the short-term forecast mode and for various scenario simulations. At the same time, the combination of different models (hydrological, atmospheric and snow cover) are expected to lead to a loss of accuracy when moving from one level to another and requires the improvement of modeling techniques.

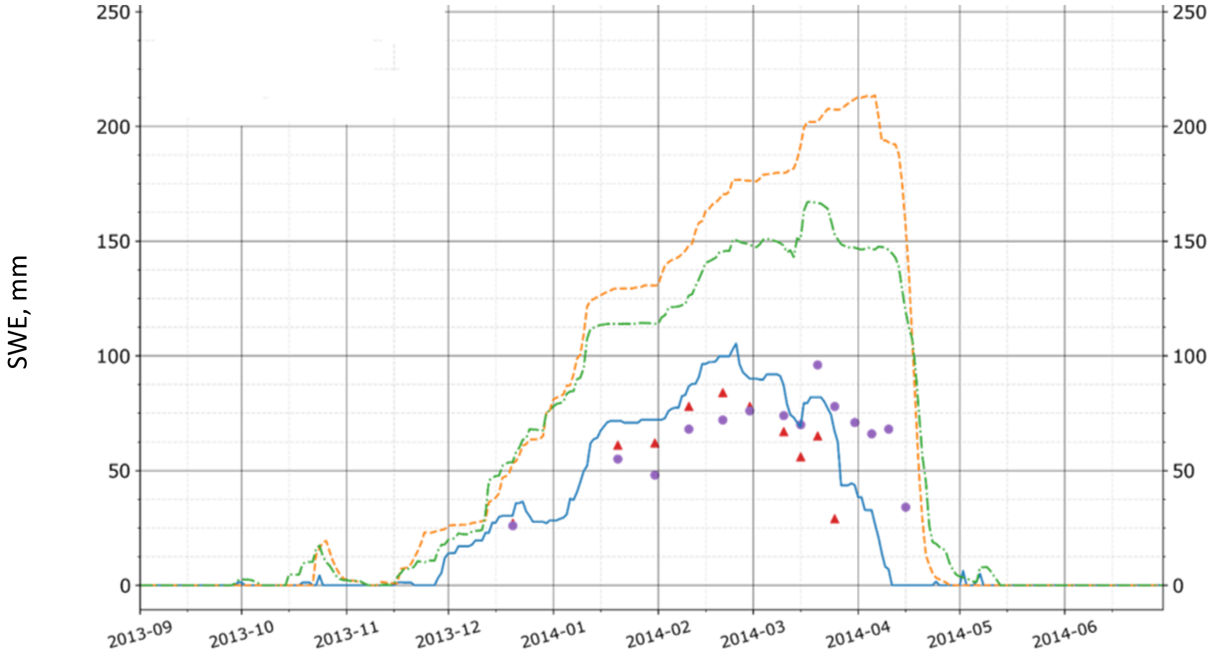

Fig. 1. Comparison of SWE for the meteorological station Syktyvkar: ICON data – yellow line, SnoWE data – blue line, ECOMAG data – green line, snow field survey –red triangles, snow forest survey – violet points

References:

1. Wilfand R M *and et al* 2014 *Non-hydrostatic system of the Hydrometeorological Center of Russia of Mesoscale Short-term Weather Forecast COSMO-Ru.* In:Turbulence, atmosphere and climate dynamics: Proceedings of the International Conference dedicated to the memory of Academician A.M. Obukhov M: GEOS) pp 265-273 (in Russian)

2. Frolova N L *and et al* 2014 *Hazard assessment of hydrological phenomena at the regional and local levels* (Russian water industry: problems, technologies, management vol 3) pp 58–74

3. Churiulin E. V. *and et al* 2018 *Analysis of snow cover characteristics by satellite and model data for different catchment areas located in the territory of the Russian Federation* (Hydrometeorological research and forecasting vol. 2) pp 120–143 (in Russian)

4. Blinov D. V., Rivin G. S. 2017 *The short-term non-hydrostatic mesoscale weather forecast system COSMO-Ru: The technological line* (Proceedings of Hydrometcenter of Russia vol. 365) pp 142–162 (in Russian)

5. *Official webpage of DWD with information about ICON*
https://www.dwd.de/EN/research/weatherforecasting/num_modelling/01_num_weather_predicti on_modells/icon_description.html

The Canadian Arctic Weather Science (CAWS) Iqaluit and Whitehorse Meteorological Supersites

Zen Mariani, Stella Melo, Paul Joe, Bob Crawford, William Burrows, Barbara Casati, Kevin Strawbridge
Environment and Climate Change Canada
Contact: zen.mariani@canada.ca

The goal of the Canadian Arctic Weather Science (CAWS) project is to conduct research into the future operational monitoring and forecasting programs of Environment and Climate Change Canada (ECCC) in the Arctic. ECCC commissioned two supersites located in Iqaluit, NU (64^{o}N, 69^{o}W) and Whitehorse, YT (61^{o}N, 135^{o}W), which are major transportation hubs that frequently experience severe weather conditions. A suite of instruments have been installed at these sites, including Ka- and X-Band radar, water vapor lidars (both in-house and commercial versions), multiple Doppler lidars, ceilometers, and radiation flux and precipitation sensors to provide automated and continuous observations of altitude-resolved winds, clouds and aerosols, visibility, radiation fluxes, turbulence, and precipitation. The benefit of integrated measurement systems at the CAWS supersites are being investigated to: 1) recommend the optimal cost-effective observing system for the Canadian Arctic that can complement existing radiosonde observations, 2) support satellite calibration and validation studies, and 3) provide enhanced meteorological observations during the World Meteorological Organization's Year of Polar Prediction (YOPP). In addition to the ground-based observations at the CAWS sites, numerical weather prediction (NWP) models have been specially configured for the Arctic and post-processed blizzard and low visibility products have been developed using artificial intelligence techniques. NWP model output at high frequency (on the order of model time-step) is also being provided from several modeling centres to enable comparisons with the CAWS supersites as part of YOPP. The full suite of instruments installed at the Iqaluit site are provided in the attached table (a similar suite of instruments has been operating at Whitehorse since 2017).

Preliminary results from the data collected at the CAWS sites show observations of unique Arctic meteorological features, including stratified layers of wind and water vapour, particularly within the boundary layer. The results clearly indicate that observational requirements for the Arctic will differ from other regions of North America. Besides the capacity to continuously monitor vertical structures in the atmosphere, the numerical model verification analysis for surface temperature indicate that turbulent flux and radiation measurements are needed to improve the quality of the local weather forecast. Processed data products from both sites are made available in near-real time to forecasters (Arctic Forecast Centres in Winnipeg and Vancouver) and other clients (Yukon Wildland Fire Management, Universities, and the general public) via the webpage ecpass.ca. Raw, unprocessed data files (ASCII or netcdf) are also available upon request.

Table: List of instruments operating at the Iqaluit supersite.

Instrument	Manufacturer	Date of Deployment	Operation	Measurement(s)	Temporal/geographic resolution
Precipitation Imaging Package (PIP)	NASA/ Wallops	Sept. 2014	380 frame/s grey-scale camera with back-lighting	Particle imagery, DSD, precip. rate and density estimation	1 min / surface obs. only
4 Cameras	Campbell Scientific	Sept. 2015	High-resolution images of the site	Ka-Radar, Lidar, and Sky-view images	5 min / 1080p
Ka-Band Radar	METEK	Sept. 2015	Scanning pulsed dual-polarization Doppler Radar	Line-of-sight wind speed and direction, cloud & fog backscatter, depolarization ratio	10 min / 10 m res. up to ~25 km range
Ceilometer CL31	VAISALA	Sept. 2015	Pulsed (8 kHz) diode laser Lidar	Cloud intensity, cloud octa and height, aerosol profiles, MLH	5 min / 5 m vert res. up to 7.5 km a.g.l.
PWD 52 Visibility Sensor (x2)	VAISALA	Sept. 2015	Forward-scatter measurement	Visibility, precipitation type	1 min / surface obs. only
Doppler Lidar	HALO	Sept. 2015	Pulsed (10 kHz) scanning at 1.5 µm (Mie scattering)	Line-of-sight wind speed and direction, aerosol backscatter, depolarization ratio	5 min / 3 m res. up to ~3 km range
Rosemount icing detector	Rosemount Engineering	Sept. 2015	Magnetostrictive oscillation probe with a sensing cylinder	Detects ice, frost	NA
Surface met obs.	Misc.	Ongoing	Misc.	Surface T, RH, pressure, winds, precipitation	1 min / surface obs. only
Radiosondes	VAISALA	Ongoing	Balloon-launched sonde	Profiles of T, RH, pressure, winds	12 hours / ~15 m res. up to ~30 km a.g.l.
4k Pantilt Camera	Axis	Oct. 2016	High-resolution images of the site	Automated pivoting camera provides images in all directions	5 min / 4k
Canadian Autonomous Arctic Aerosol Lidar (CAAAL)	ECCC	Oct. 2016	355/532/1064 nm transmitter & 6 ch. receiver	Aerosol and water vapour profiles; particle size and shape information	1 min / 3 m res. up to ~15 km a.g.l.
Doppler Lidar x2: Ridge (T121)	HALO	Oct. 2017	Pulsed (10 kHz) scanning at 1.5 µm (Mie scattering)	Line-of-sight wind speed and direction, aerosol backscatter, depolarization ratio	5 min / 3 m res. up to ~3 km range
Fog Measuring Device (FMD)	DMT	Sept 2018	Fog sensor	Fog intensity, water vapour at surface	1 min / NA
Far-IR Radiometer (FIRR)	LR Tech.	Sept 2018	Zenith/Nadir-viewing infrared radiometer	Downwelling IR radiation, cloud microphysics	2 min / NA
Surface radiation fluxes	Campbell Scientific	Sept 2018	Surface radiation sensors (diffuse and direct)	Short- and long-wave up, down, and horizontal radiation	1 min / NA
Water Vapour Lidar	VAISALA	Sept 2018	Pulsed DIAL lidar system	Profiles of aerosols, 24-hr water vapour profile	20 minutes / 5 m up to ~3 km agl (WV)

Link of the Arctic and Antactic sea ice extent with El Niño phenomena

I.I. Mokhov[1,2] and M.R. Parfenova[1]

[1]A.M. Obukhov Institute of Atmospheric Physics RAS
[2]Lomonosov Moscow State University
mokhov@ifaran.ru, parfenova@ifaran.ru

The most rapid current climate changes are detected in the Arctic. One of key features of the contemporary changes is the rapid reduction of the Arctic sea ice extent. Very diverse variations were detected during the last decades for Antarctic sea ice extent with significant changes in behavior during the recent years. The strongest interannual variations of the global climate are associated with El-Niño phenomena, and it is natural to expect the manifestation of El-Niño effects in different latitudes, including high latitudes [1,2]. Here we estimate the relationship of changes of the Arctic (ArcSIE) and Antarctic (AntSIE) sea ice extents since 1980s (http://nsidc.org) and their links with El-Niño phenomena of various types characterized by different indices (Niño3 and Niño4) with the use of cross-wavelet analysis.

Figure 1 shows local coherence of Arctic and Antarctic sea ice extent from monthly-mean satellite data for the period 05.1988-04.2019. According to Fig. 1, the correlation for interannual variations of ArcSIE and AntSIE since 2000s is displayed, along with their anti-correlation in the annual cycle. The most significant coherence between ArcSIE and AntSIE is noted for the variations with the periods of about 5 years, characteristic for El Niño phenomena. It is worth to note positive correlation of ArcSIE and AntSIE for intra-annual (semi-annual) variations.

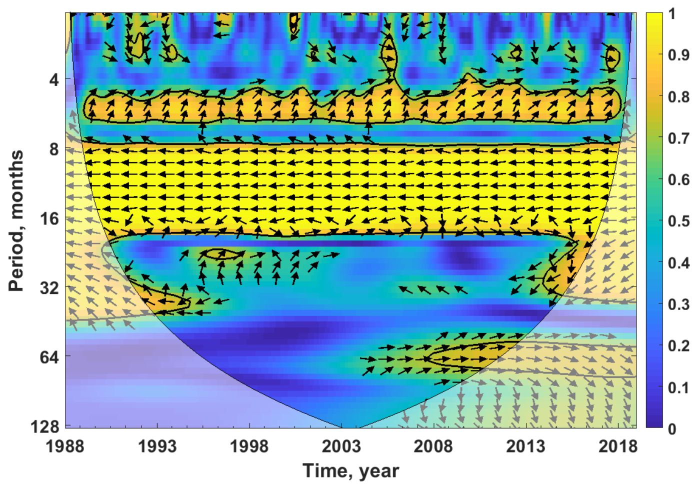

Fig. 1. Local coherence of Arctic and Antarctic sea ice extent by monthly-mean satellite data for the period 05.1988-04.2019.

Figure 2 shows local coherence of Arctic sea ice extent with El Niño indices Niño3 and Niño4 by monthly-mean satellite data for the period 05.1988-04.2019. During the last decade, the significant positive correlation between ArcSIE and both El Niño indices variations for intra-decadal variations with the periods of about 5 years (characteristic for El Niño phenomena) is observed. On the other hand, the significant differences in coherence of decadal and interdecadal ArcSIE variations with Niño3 and Niño4 are displayed. The decadal and interdecadal AntSIE variations show negative correlation with El Niño indices (significant with Niño3 and insignificant with Niño4) during last decades.

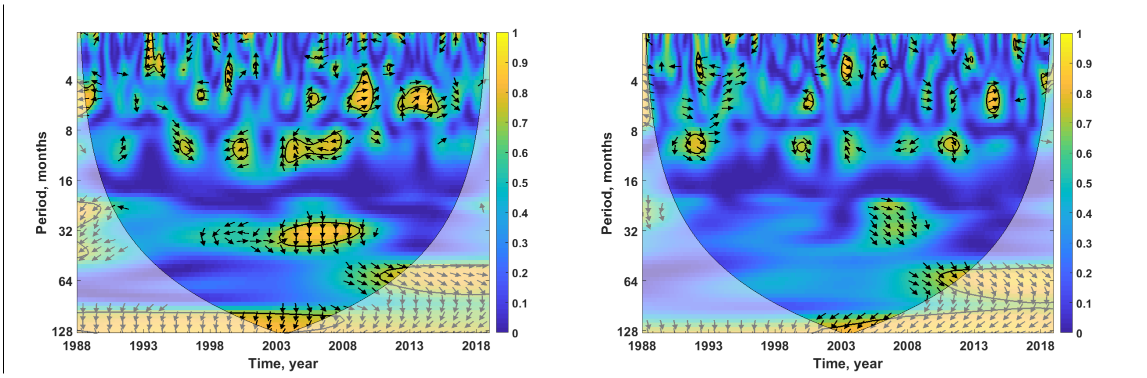

Fig. 2. Local coherence of Arctic sea ice extent with El Niño indices Niño4 (left) and Niño3 (right) by monthly-mean satellite data for the period 05.1988-04.2019.

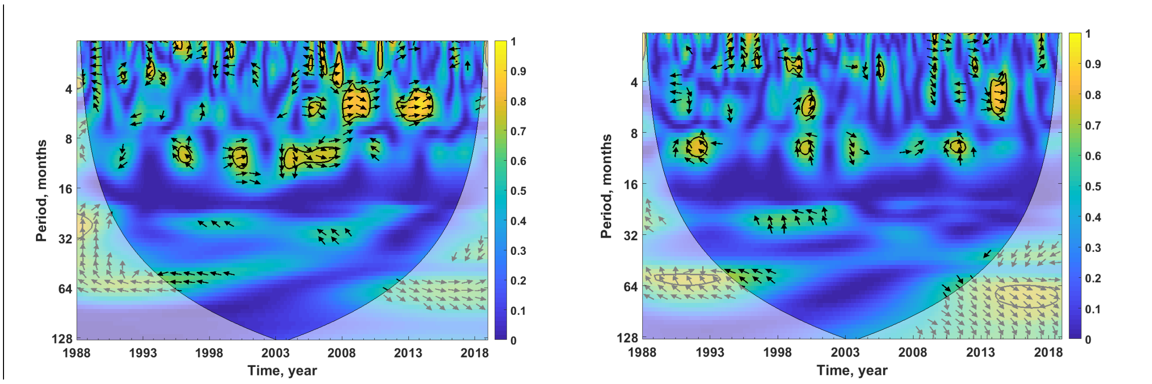

Fig. 3. Local coherence of Antarctic sea ice extent with El Niño indices Niño4 (left) and Niño3 (right) by monthly-mean satellite data for the period 05.1988-04.2019.

Figure 3 shows local coherence of Antarctic sea ice extent with El Niño indices Niño3 and Niño4 by monthly-mean satellite data for the period 05.1988-04.2019. According to Fig. 2 and Fig. 3, the AntSIE coherence with El Niño indices is overall less significant than the ArcSIE coherence. The coherence of AntSIE interannual variations with El Niño indices (especially with Niño3) is displayed during last years.

This work has been supported by the RSF (project No. 19-17-00240) using the results obtained in the framework of the RAS Presidium program "Climate change: causes, risks, consequences, problems of adaptation and regulation" and RFBR (projects No. 17-05-01097 and No. 18-05-60111).

References

1. Mokhov I.I. Contemporary climate changes in the Arctic. *Herald Russ. Acad. Sci.,* 2015, **85** (3), 265–271.
2. Mokhov I.I., Parfenova M.R. Link of the Barents Sea ice extent with El-Nino phenomena. *Research activities in Atmospheric and Oceanic Modelling*, E. Astakhova (ed.), 2018, Rep. No 48, WCRP Rep. No 15/2018, 2.17-2.19.

Changes of the Selenga River runoff in the Lake Baikal basin and their relationship to El Niño phenomena

I.I. Mokhov[1,2] and M.R. Parfenova[1]

[1]A.M. Obukhov Institute of Atmospheric Physics RAS
[2]Lomonosov Moscow State University
mokhov@ifaran.ru, parfenova@ifaran.ru

The Lake Baikal basin is among North Asian regions with the strongest warming in summer during the last decades. Long-term positive trends of surface air temperature in the region are accompanied by negative trends for precipitation during the last decades (http://meteorf.ru/). Such regional climate trends should cause negative trends of the water balance in the Lake Baikal basin. Against the background of long-term trends, significant interannual climate variations are revealed. In particular, the summer of 2015 was characterized by extremely high temperature and extreme precipitation deficit in the Lake Baikal basin. It can be related with the influence of the strongest El Nino that year [1-8]. We assess here the relationship of the runoff of the Selenga River (as a key water supplier to Lake Baikal) to the El Nino phenomena with the use of cross-wavelet analysis of observations for the period 1934-2015. Different El Nino indices were used to account for different types of El Niño.

Figure 1 shows local coherences of the Selenga River runoff in July with the El Nino indices Nino4 (a) and Nino3 (b) in January for the period 1934-2015. According to Fig. 1 there is significant coherence of the Selenga River runoff in summer with both El Nino indices in preceding winter since 1990s on intra-decadal time scale. There is a significant difference in interdecadal (long-term) coherence for different El Nino indices. Figure 1a shows significant relationship between long-period variations of the Selenga River runoff with Nino4 index since the second half of 1970s. At the same time, Figure 1b does not show any significant coherence between long-period variations of the Selenga River runoff with Nino3 index.

(a) (b)

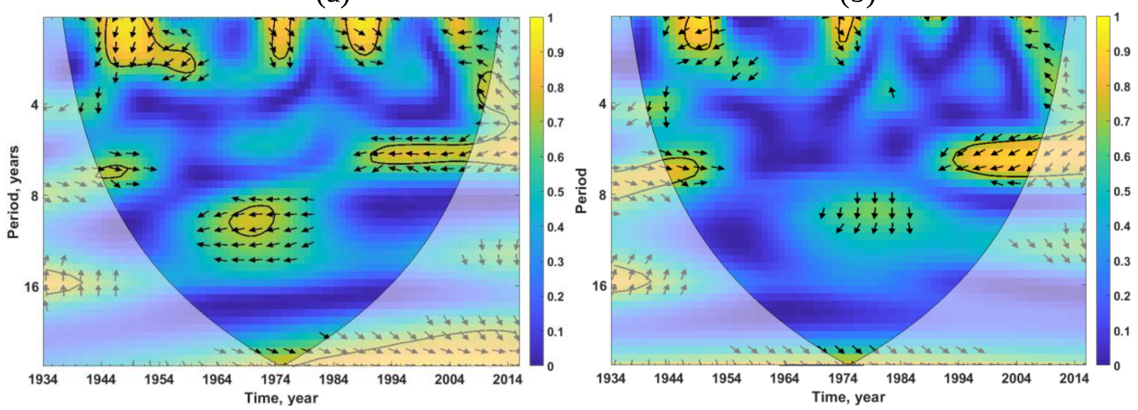

Fig. 1. Local coherences of the Selenga River runoff in July with the El Nino indices Nino4 (a) and Nino3 (b) in January for the period 1934-2015. The arrows signify the correlation phase direction.

Figure 2 shows local coherences of the Selenga River annual-mean runoff with El Nino indices Nino4 (a) and Nino3 (b) in January for the period 1934-2015. According to Fig. 2 in comparison with Fig.1 there is less significant coherence between both El Nino indices in winter and Selenga River annual-mean runoff since 1990s on intra-decadal time scale.

(a) (b)

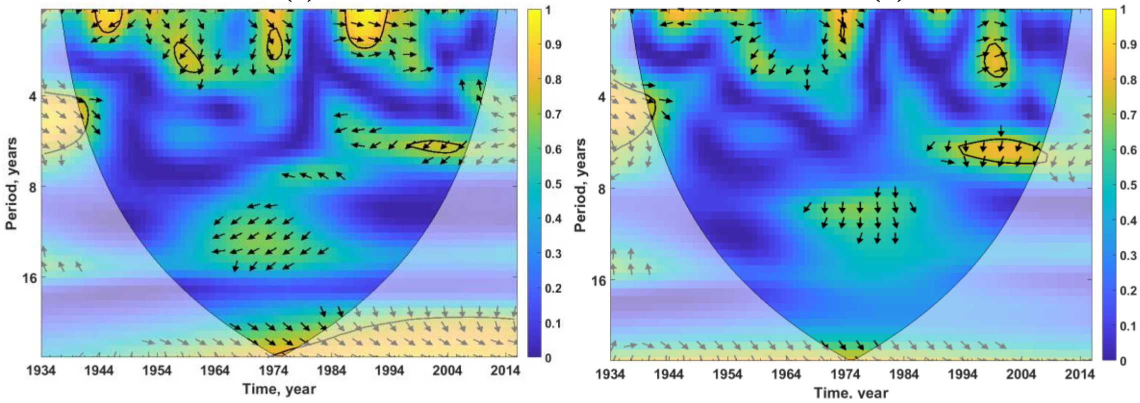

Fig. 2. Local coherences of the Selenga River annual-mean runoff with the El Nino indices Nino4 (a) and Nino3 (b) in January for the period 1934-2015.

We thank V.Yu. Georgievsky for the help in obtaining data for the Selenga River runoff. This work has been supported by the RSF (project No. 19-17-00240). The results obtained in the framework of the RAS Presidium program "Climate change: causes, risks, consequences, problems of adaptation and regulation" and RFBR (projects No. 17-05-01097 and No. 17-29-05098) were used.

References

1. Mokhov I.I., J.-L. Dufresne, Le Treut H., V.A. Tikhonov and A.V. Chernokulsky, 2005: Changes in drought and bioproductivity regimes in land ecosystems in regions of Northern Eurasia based on calculations using a global climatic model with carbon cycle. *Doklady Earth Sci.*, **405A**(9), 1414-1418.
2. Khon V.C. and I.I. Mokhov, 2012: The hydrological regime of the largest rivers basins of northern Eurasia in XX-XXI centuries. *Water Res.*, **39**(1), 3-12.
3. Mokhov I.I., 2014: Hydrological anomalies and tendencies of change in the basin of the Amur River under global warming. *Doklady Earth Sci.*, **455**(2), 459-462.
4. Mokhov I.I., V.C. Khon, A.V. Timazhev, A.V. Chernokulsky and V.A. Semenov, 2014: Hydrological anomalies and trends in the Amur River Basin due to climate change. In: *Extreme Floods in the Amur River Basin: Causes, Forecasts, and Recommendations*, Moscow, Roshydromet, 81-120. (in Russian)
5. Mokhov I.I. and A.V. Timazhev, 2015: Estimates of the predictability of climate anomalies in the Russian regions due to the El Niño. *Doklady Earth Sci.*, **464**(6), 722-726.
6. Mokhov I.I. and A.V. Timazhev, 2016: Climate anomalies and tendencies of change in Lake Baikal basin. *Research Activities in Atmospheric and Oceanic Modelling*, E. Astakhova (ed.), WCRP Rep. No.15/2016, S. 2, P. 9–10.
7. Mokhov I.I. and A.V. Timazhev, 2016: Summer climate anomalies in the Northern Eurasia during intra-annual transitions from El Niño to La Niña. *Research Activities in Atmospheric and Oceanic Modelling*, E. Astakhova (ed.), WCRP Rep. No.15/2016, S. 6, P. 7–8.
8. Mokhov I.I. and A.V. Timazhev, 2016: Weather-climate anomalies in Russian regions: El Niño-associated predictability. *Research Activities in Atmospheric and Oceanic Modelling*, E. Astakhova (ed.), 2016, WCRP Rep. No.15/2016, S. 6, P. 9–10.

Long-term variations in relationships of ionospheric F2-layer parameters based on different solar activity indices

Mokhov I.I.[1,2]
[1]A.M. Obukhov Institute of Atmospheric Physics RAS
[2]Lomonosov Moscow State University
mokhov@ifaran.ru

Studies of long-term changes in the middle and upper atmosphere, including ionosphere, are significant for the detection of changes in the Earth climate system, including diagnostics of relative role of natural and anthropogenic factors [1-8]. Significant ionospheric characteristics are critical frequency of the F2 layer on its height h_mF2. The change in the dependence of the critical frequency of the F2 layer on its height h_mF2 was considered in [6] on the basis of two sources of initial data. It was found that the slope k of the dependence of *fo*F2 on h_mF2 systematically decreases from the earlier period (1958–1980) to the later periods (1988–2010, 1998–2010, 1998–2014). According to obtained results the detected decrease in k confirms the concept of the decrease in the concentration of atomic oxygen in the thermosphere since the value of f_oF2 depends much more on the concentration of atomic oxygen in the F region than h_mF2. Here, the relationships of different ionospheric parameters and their variations are studied with the use of cross-wavelet analysis of global-scale data for the period 1948-2009 [4,5]. In particular, similar to [5] two data sets for f_oF2 and h_mF2 (derived from M(3000)F2) based on solar 10.7 cm radio flux F10.7 (data set I) and based on the solar sunspot number R (data set II) have been used.

Figure 1 shows local coherence between h_mF2 and *fo*F2 (data set I) for 1948-2009 with an intervals of significant positive correlation of h_mF2 and *fo*F2 interannual and interdecadal variations. There is a significant coherence for quasi-decadal variations of h_mF2 and *fo*F2 with a decrease in significance since the end of 1990s. Significant coherence was noted for intra-decadal variations in the 1970s (till the early 1980s). It should be noted that no long-term coherence was revealed.

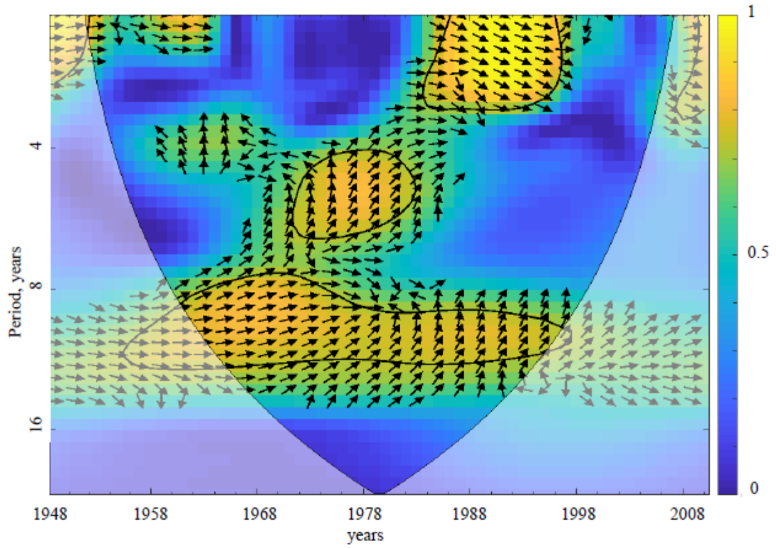

Fig. 1. Local coherence between h_mF2 and *fo*F2 (data set I) during the period 1948-2009.

Figure 2 shows local coherence between different data series (I and II) for h_mF2 for the period 1948-2009. There is a significant coherence of long-term (inter-decadal) variations for two data series of h_mF2. The time intervals with significant positive correlation for decadal and intra-decadal variations alternate with intervals of its lack. The only regime with significant negative correlation was noted for intra-decadal variations in the time interval from the second half of 1970s till the beginning of 1980s.

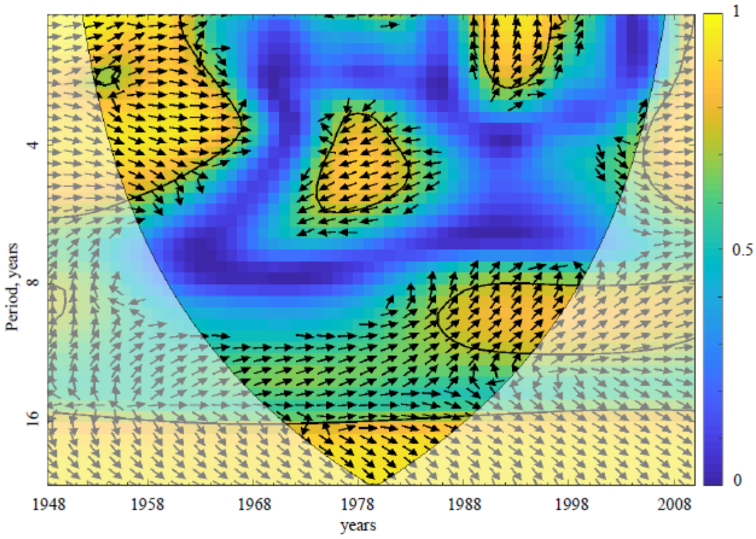

Fig. 2. Local coherence between different data series (I and II) for h_mF2 for the period 1948-2009.

The local coherence between different data series (I and II) for *fo*F2 during 1948-2009 was obtained substantially weaker than for h_mF2. For the second data set (II), the coherence between h_mF2 and *fo*F2 during 1948-2009 was also estimated as a whole substantially weaker than for the first data set (I).

This work was supported by the RSF (project No. 19-17-00240). The results obtained in the framework of the RAS Presidium program "Climate change: causes, risks, consequences, problems of adaptation and regulation" and RFBR (projects No. 17-05-01097 and No. 17-29-05098) were used.

References

1. Roble R.G., Dickinson R.E. How will changes in carbon dioxide and methane modify the mean structure of the mesosphere and thermosphere?, Geophys. Res. Lett., 1989, **16**, 1441–1444.

2. Rishbeth H. A greenhouse effect in the ionosphere? Planet. Space, 1990, **38**, 945-948.

3. Rishbeth H., Roble R.G. Cooling of the upper atmosphere by enhanced greenhouse gases - Modelling of thermospheric and ionospheric effects. Planet. Space, 1992, **40**, 1011-1026.

3. Golitsyn G.S., Semenov A.I., Shefov N.N., Fishkova L.M., Lysenko E.V., Perov S.P. Long-term temperature trends in the middle and upper atmosphere, Geophys. Res. Lett., 1996, **23**, 1741-1744.

4. Damboldt T., Suessmann P. Consolidated database of worldwide measured monthly medians of ionospheric characteristics f_oF2 and M(3000)F2. INAG Bull. On the Web, INAG-73, www.ips.gov.au/IPSHosted/INAG/web-73/index.html, 2012.

5. Mielich J., Bremer J. Long-term trends in the ionospheric F2 region with different solar activity indices. Ann. Geophys., 2013, **31**, 291-303.

6. Danilov A.D., Konstantinova A.V. Long-term changes in the relation between f_oF2 and h_mF2. Geomagn. Aeron., 2016, 56 (5), 577-584.

7. Laštovička J. A review of recent progress in trends in the upper atmosphere. J. Atmos. Solar-Terr. Phys., 2017, **163**, 2-13.

8. Mokhov I.I., Semenov A.I., Volodin E.M., Dembitskaya M.A. Changes of cooling near mesopause under global warming from observations and model simulations. Izvestiya, Atmos. Oceanic Phys., 2017, **53** (4), 383–391.

Variations in links of key modes of interdecadal climate variability with El Niño phenomena

M.R. Parfenova[1] and I.I. Mokhov[1,2]

[1]A.M. Obukhov Institute of Atmospheric Physics RAS
[2]Lomonosov Moscow State University
parfenova@ifaran.ru, mokhov@ifaran.ru

The strongest interannual variations of the global climate are associated with El Niño phenomena. Significant interdecadal global-scale climate variations are associated with oscillations like Atlantic Multidecadal Oscillation (AMO), Pacific Decadal (PDO) and Interdecadal Pacific (IPO) Oscillations. Different mechanisms are responsible for generation of various key interannual and interdecadal climate oscillations and their variations and links. Here we study variations in links with El Niño phenomena of key modes of interdecadal climate variability since the beginning of the 20th century with the use of the cross-wavelet analysis of data from (https://climexp.knmi.nl/). This analysis is performed with different El Niño indices characterizing different El Niño types.

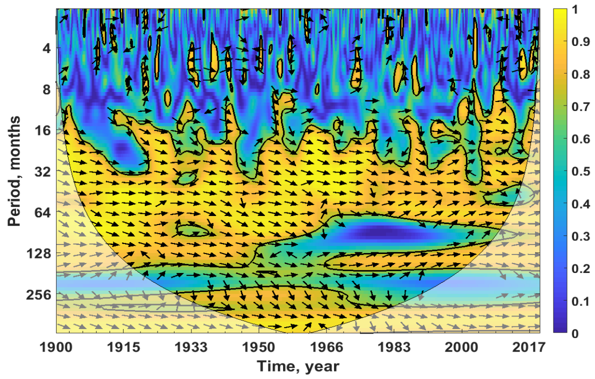

Figure 1. Local coherence between Nino3 and Nino4 indices of El Niño phenomena by monthly-mean data for the period 1900-2019. The arrows signify the correlation phase direction.

Figure 1 shows the coherence between El Niño phenomena characterized by Nino 3 and Nino 4 indices from monthly-mean satellite data for the period 1900-2019. Significant coherence between Nino3 and Nino4 is noted for intra-decadal variations with a period about 5 years, characteristic for El Niño phenomena, and for long-term variations with a period larger than two decades. The coherence for decadal variations is less significant as a whole.

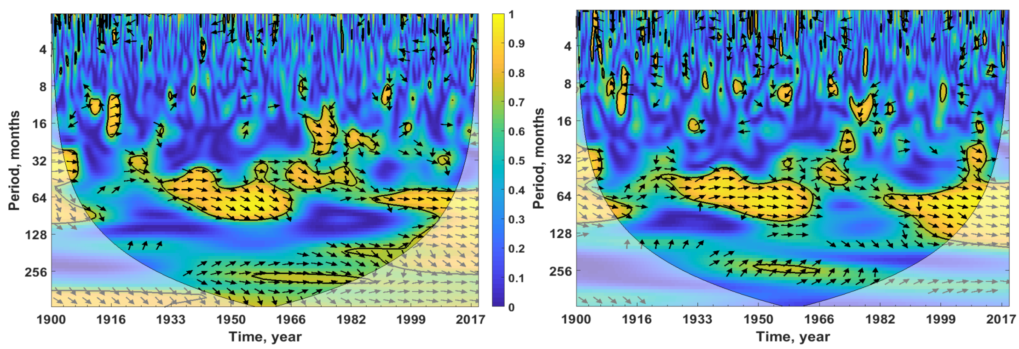

Figure 2. Local coherence of Nino3 (left) and Nino4 (right) indices of El Niño phenomena and PDO by monthly-mean data for the period 1900-2018. The arrows signify the correlation phase direction.

Figure 2 shows local coherence between El Niño phenomena (Nino 3 and Nino 4 indices) and PDO by monthly-mean data for the period 1900-2018. The most significant coherence between El Niño (Nino3 and Nino4) and PDO is observed for variations with periods of about 5 years, characteristic for El Niño phenomena. The coherence of PDO and El Niño phenomena for decadal and interdecadal variations is more significant in the case when El Niño phenomena are characterized by Nino3 index.

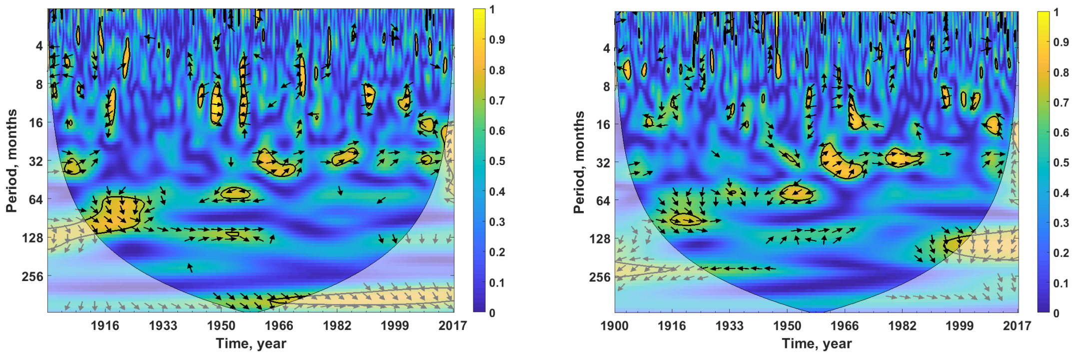

Figure 3. Local coherence of Nino3 (left) and Nino4 (right) indices of El Niño phenomena and IPO by monthly-mean data for the period 1900-2016. The arrows signify the correlation phase direction.

Figure 3 shows the coherence between Nino3 and Nino4 indices and IPO for the period 1900-2016 by monthly mean data. Along with interannual local coherence, 5 years local coherence can be spotted, and, at the same time, 10 years coherence with Nino4 is noted in recent years.

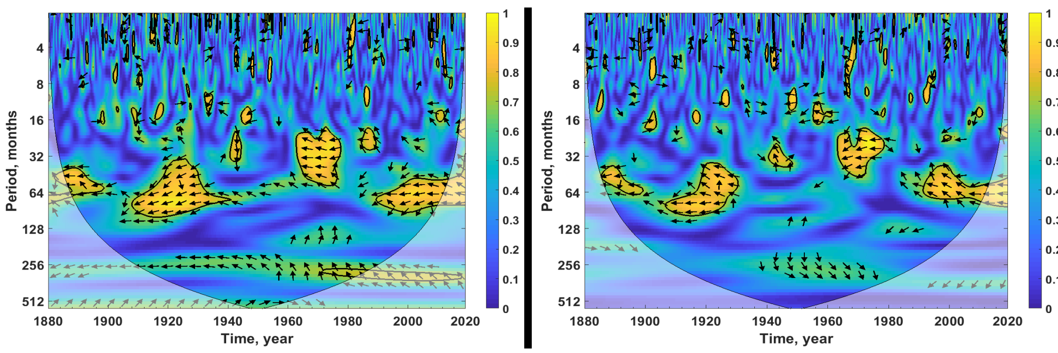

Fig. 4. Local coherence of the indices Nino3 (left) and Nino4 (right) of El Niño phenomena with AMO by monthly-mean data for the period 1880-2019. The arrows signify the correlation phase direction.

Figure 4 displays local coherence of El Niño phenomena (Nino3 and Nino4 monthly-mean indices) with AMO for the period 1880-2019. Time intervals with significant anticorrelation are exhibited for the typical for El Niño phenomena 5-year period. Significant anticorrelation is displayed also between El Niño phenomena (characterized by Nino3 index) and AMO for variations with a period about two decades since 1970s.

This work was supported by the RSF (project No. 19-17-00240). The results obtained withinin the framework of the RAS Presidium program "Climate change: causes, risks, consequences, problems of adaptation and regulation" and RFBR (projects No. 17-05-01097 and No. 17-29- 05098) were used.

Trends in the occurrence of Australian northwest cloudbands

Reid, K. J., I. Simmonds, C. L. Vincent and A. D. King
School of Earth Sciences, The University of Melbourne, Victoria 3010, Australia
simmonds@unimelb.edu.au

The Australian Northwest Cloudband (NWCB) is a commonly-occurring continental-scale band of continuous cloud that stretches from northwest to southeast Australia. A typical example is presented in Fig. 1. They are associated with numerous weather features across the continent, including precipitation events.

We have developed an automatic algorithm to identify these features, and have applied it to once-per-day data of the recently-released H-Series product of the International Satellite Cloud Climatology Project (ISCCP) (Young et al., 2018) for the period 1984-2014. Fig. 2 shows the time series of cloud band counts for each season and for the annual total. It shows that there has been an increase in the number of these features in all seasons. All the trends are statistically different from zero ($p < 0.05$) except for those in autumn and winter.

We are exploring how the occurrence and structure of the cloudbands is associated with the regional scale circulation and its trends. This is being undertaken with the ERA-Interim reanalysis dataset (Dee et al. 2011).

Further details of this investigation can be found in Reid et al. (2019).

References

Dee, D. P., et al., 2011: The ERA-Interim reanalysis: Configuration and performance of the data assimilation system. *Quart. J. Roy. Meteor. Soc.*, **137**, 553-597, doi: 10.1002/qj.828.

Reid, K. J., I. Simmonds, C. L. Vincent and A. D. King, 2019: The Australian northwest cloudband: Climatology, mechanisms and association with precipitation. *J. Climate*, (under review).

Young, A. H., K. R. Knapp, A. Inamdar, W. Hankins and W. B. Rossow, 2018: The International Satellite Cloud Climatology Project H-Series climate data record product. *Earth System Science Data*, **10**, 583-593, doi: 10.5194/essd-10-583-2018.

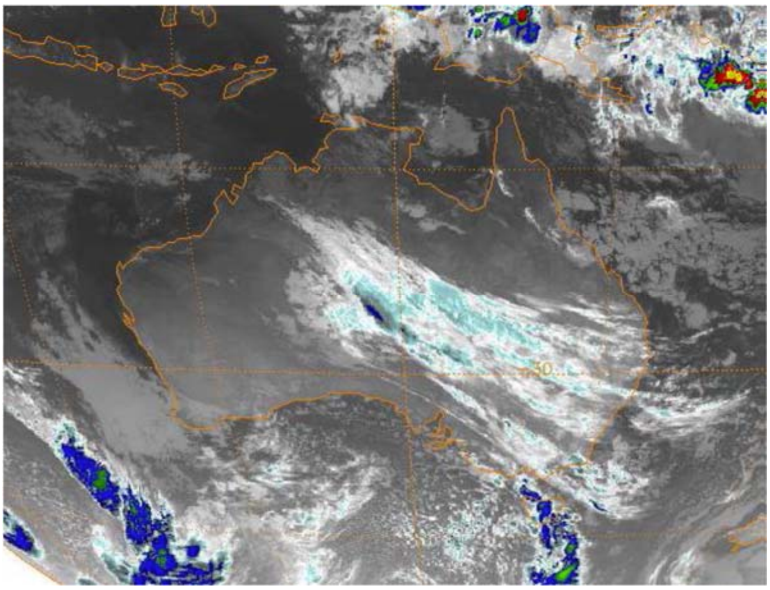

Fig. 1: Typical NWCB. 13 June, 1994, 12UTC (IR image from GMS-4).

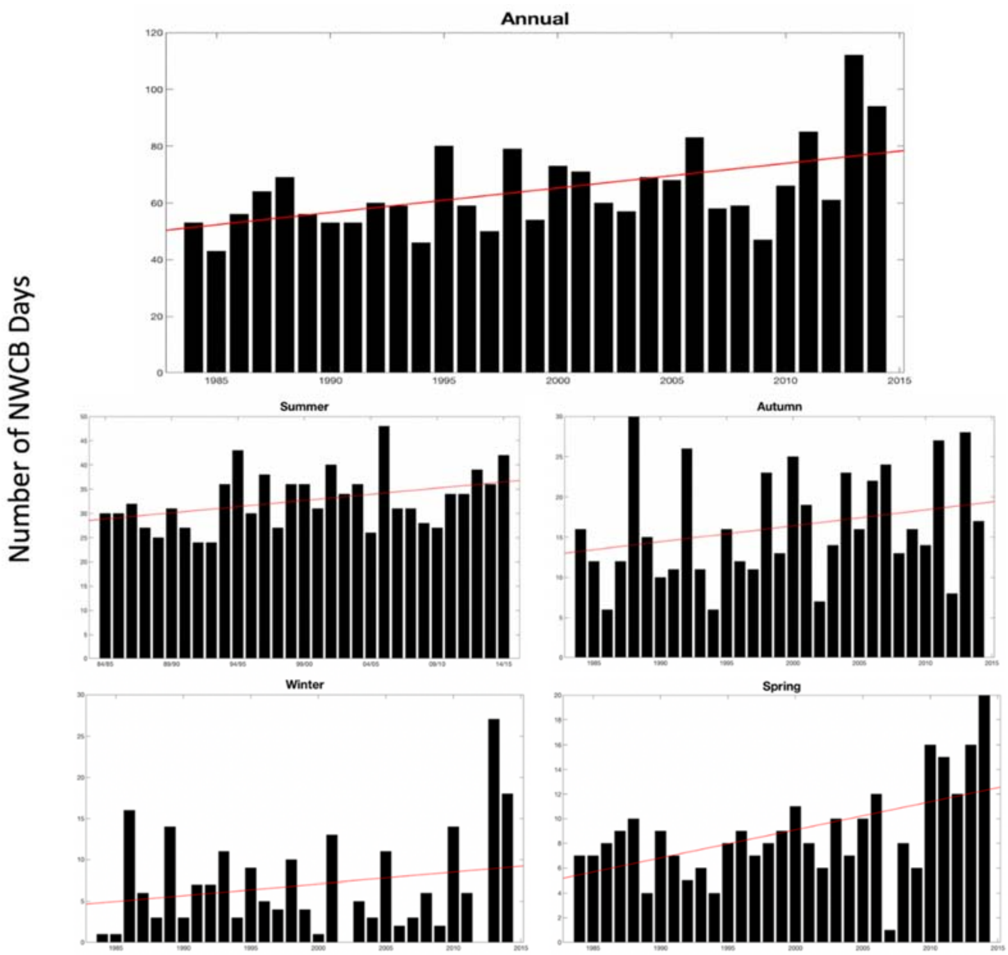

Fig. 2: Timeseries of the mean annual and seasonal number of NWCB days 1984-2014. The lines of least-squares best fit are indicated.

Southern Hemisphere fronts and their role in changes in the Hadley Cell extent

Irina Rudeva[1], Ian Simmonds[1], David Crock[2] and Ghyslaine Boschat[3]

[1]School of Earth Sciences, The University of Melbourne, Victoria 3010, Australia
simmonds@unimelb.edu.au
[2]Bureau of Meteorology, Brisbane, Queensland, Australia
[3]School of Earth, Atmosphere and Environment, Monash University, Clayton, Victoria, Australia

A notable feature of global circulation is the 'seamless' meridional transport of moist static energy towards the poles. In the tropics this transport is predominantly effected by the Hadley Circulation (HC), and by baroclinic transient eddies in the extratropics. The seamless character means that there is an intimate connection between variation in the HC and the midlatitude eddies. In recent times considerable focus has been placed on the expansion of the HC (e.g., Grise et al. (2019)) and we are exploring the involvement of SH fronts in that change.

Our analysis is based on the ERA-Interim reanalysis (Dee et al. 2011). The edge of the SH HC is taken to be the location of the subtropical ridge (STR), while frontal features are determined with the automated scheme described by Simmonds et al. (2012) and Rudeva and Simmonds (2015). Fig. 1 shows the strong geographical connections between the STR and front frequency.

In five key sectors of the SH (see Fig. 1) the lead/lag correlations between the daily counts of fronts lying in 20-40°S and STR latitude (STRP) are calculated. (Similar calculations are performed for STR intensity (STRI).) In the annual case (Fig. 2) the STRP (significant) correlations peak when frontal counts lead STRP by about 1 day. A similar, but less clear, situation applies to STRI. The results suggest that in this context midlatitude changes *lead* those of the HC. Further details appear in Rudeva et al. (2019).

References

Dee, D. P., et al., 2011: The ERA-Interim reanalysis: Configuration and performance of the data assimilation system. *Quart. J. Roy. Meteor. Soc.*, **137**, 553-597.

Grise, K. M., et al., 2019: Recent tropical expansion: Natural variability or forced response? *J. Climate*, **32**, 1551-1571.

Rudeva, I., and I. Simmonds, 2015: Variability and trends of global atmospheric frontal activity and links with large-scale modes of variability. *J. Climate*, **28**, 3311-3330.

Rudeva, I., et al., 2019: Midlatitude fronts and the variability in the Southern Hemisphere tropical width. *J. Climate*, (under review).

Simmonds, I., et al., 2012: Identification and climatology of Southern Hemisphere mobile fronts in a modern reanalysis. *J. Climate*, **25**, 1945-1962.

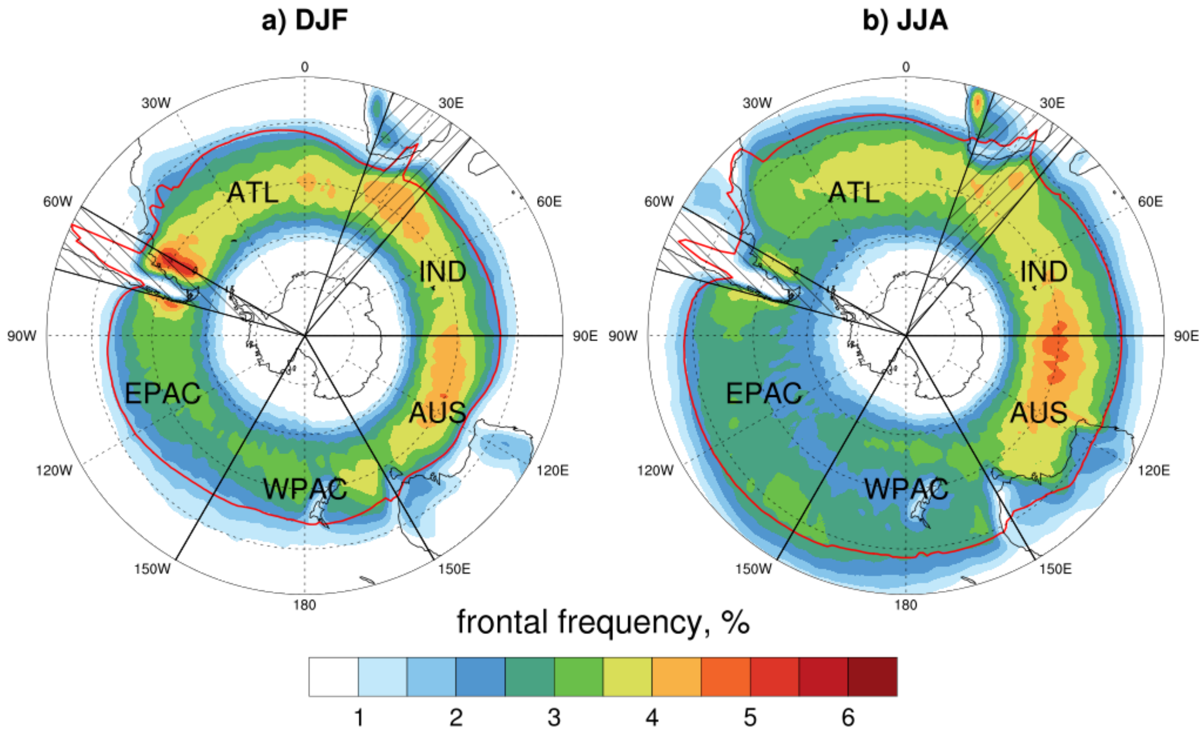

Fig. 1: Climatological frontal frequency (color; %) and the mean STR position (red line) in (a) DJF and (b) JJA averaged over a 30-year period (1980–2009 and 1979–2008, respectively).

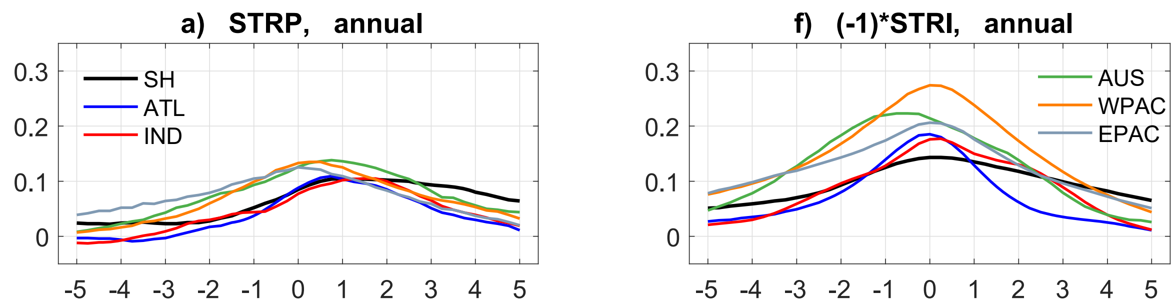

Fig. 2: Lag-correlation between the number of fronts in the SH and (left) STRP and (right) STRI. Positive lag times indicate that the number of fronts *leads* the changes in STR characteristics.

The scale-dependency of the signal-to-noise ratio in a regional oceanic system

Shengquan Tang(1, 2), Hans von Storch (1, 2) and Xueen Chen(1)
(1) Ocean University of China, Qingdao, P. R. China
(2) Institute of Coastal Research, HZG, Geesthacht, Germany
Email: 2277520917@qq.com, hvonstorch@web.de, xchen@ouc.edu.cn

The internal variability is ubiquitous in the climate system; it emerges at all locations and times, at all scales (von Storch et al., 2001, Hasselmann, 1976). Tang et al. (2019) demonstrated the existence of the internal variability in a regional oceanic system., namely the South China Sea. Here, we conceptualize the variability coming from the external forcing as "signal", and the variability coming from the internal variability as "noise".

By using an ensemble of four simulations of the flow in the South China Sea with the same ocean models exposed to the same atmospheric forcing as recorded in 2008, which differ only in the initial conditions, the scale-dependency of the signal-to-noise (S/N) ratio of the barotropic flow is studied. The barotropic velocities is stored one per day. Although these members are almost identical except the initial condition, there are significant notable differences between the.

The "signal" is measured by the ensemble mean computed as $\mu(t)=\langle X(t)\rangle$. The "noise" is measured by the standard deviation σ between the four members of the ensemble, i.e., by $\sigma(t) = \sqrt{\left(\sum_{i=1}^{4}(X_i(t) - \mu(t))^2\right)/4}$. Thus, the S/N ratio is the ratio between the standard deviation of the time series of $\mu(t)$ across 2008, and the standard deviation $\sigma(t)$ of the variations relative to $\mu(t)$ in 2008.

For studying the scale dependency of the S/N ratio, we determine first the EOFs of the daily barotropic velocity potential across all four 2008-simulations. The EOFs are ranked as usual, with an index sorted according to the percentage of explained variance. An inspection of the patterns reveals that low-indexed EOFs go with large scales, medium-indexed EOFs with medium scales and high-indexed one with small scales. Thus, principal components of these EOFs are associated with scales, which decrease with increasing indices of the EOFs.

Figure 1 shows the distribution of the S/N ratio as a function of the index of EOFs. We find that the S/N ratios decline with the increases of the EOFs-indices. This means that the variability of the large-scale components of the barotropic ocean dynamics is mainly controlled by the external forcing while the influence of internal variability is mostly negligible, in other words - the S/N ratio is high. On the other hand, the small-scale barotropic dynamics is associated with small S/N ratios, which indicates that the external forcing is weak and internal variability is dominant,

Based on the distribution of the S/N ratio, we divide the scales in three boxes, EOF 1-10, EOF 11-50 and EOF 50-1400.Then in order to get the map of the S/N ratio, we use the daily barotropic states for the range of EOFs as X at each point for computing the S/N ratio (Figure 2).

By studying the scale-dependency of the S/N ratio, this work demonstrates that the small-scale variability in the South China Sea is not only influenced by the external forcing but also by the internal variability. The significance of the externally driven component, and of the internally driven component, changes with the scale; the larger the scale, the more important the external forcing, the smaller the scale, the more the internal generated variability.

Tang, S., von Storch, H., Chen, X., & Zhang, M. (2019). “Noise” in climatologically driven ocean models with different grid resolution. Oceanologia, 61(3), 300–307. https://doi.org/10.1016/j.oceano.2019.01.001.

von Storch, H., von Storch, J.-S., Müller, P., 2001. Noise in the climate system –ubiquitous, constitutive and concealing. In: Engquist, B., Schmid, W. (eds.), Mathematics Unlimited – 2001 and Beyond. Part II. Springer Verlag, Berlin, Heidelberg, 1179–1194, https://dx.doi.org/10.1007/978-3-642-56478-9_62.

Hasselmann, K., 1976: Stochastic climate models. Part I. Theory. *Tellus* 28, 473-485

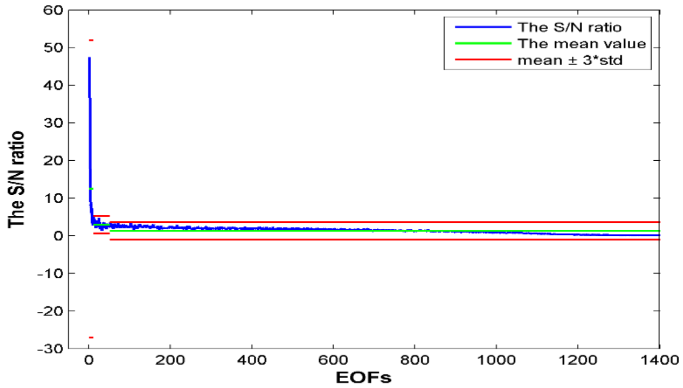

Figure 1 The S/N ratios as a function of EOF index. Small scales are situated at the right end, large-scales at the left end. Based on the distribution of the S/N ratio, the scales (EOFs) are divided into three boxes, EOF 1-10, EOF 11-50 and EOF 51-1400. The green line in each box is the mean value of the ratio values, and the red lines above and below the green line in each box are the mean value ± 3 standard deviation of the S/N ratio in the same box, respectively.

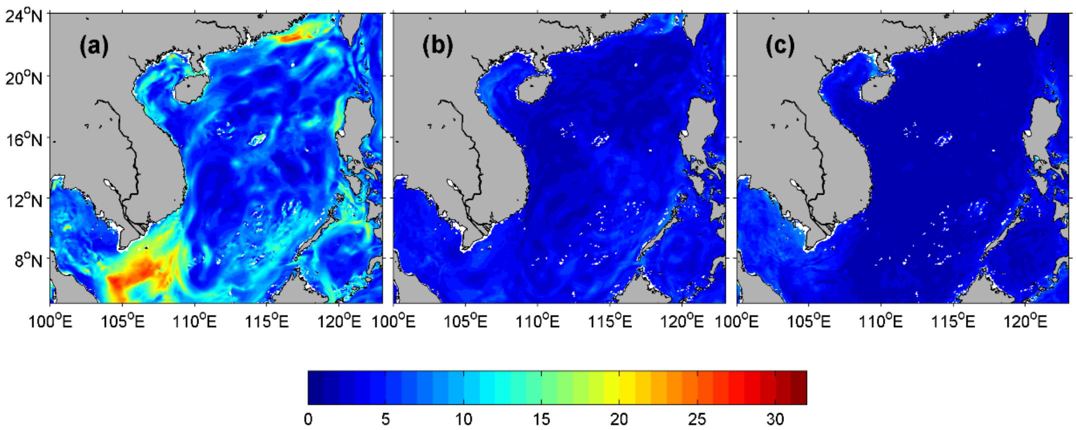

Figure 2 Maps of the S/N ratio for (a) the first box EOF 1-10, (b) the second box EOF 11-50, (c) the third box EOF 51-1400.

Coupled changes in Antarctic sea ice and cyclones on the daily time scale

Dominic B. Thorn, Ian Simmonds and Andrew D. King

School of Earth Sciences, The University of Melbourne, Victoria 3010, Australia
simmonds@unimelb.edu.au

Many studies have explored to association Antarctic sea ice and large-scale atmospheric circulation features (e.g., Pezza et al.), but most of these focus on scales longer than the synoptic time scale. Because of inherent nonlinearities there is an argument to be made for examining those links on daily timescales. Here we identify cyclones with the Melbourne University algorithm (see Grieger et al. (2018)) and apply it to the ERA-I reanalysis (Dee et al., 2011). Sea ice data are taken from the NSIDC NASA Team passive microwave data. The mean seasonal sea ice edge from these data are shown in Fig. 1.

We split the Southern Ocean (south of 55°S) into nine 40°-wide sectors (indicated in Fig. 1). For each sector we calculate the ice extent (SIE). To investigate its day-to-day variability we define ΔE as the daily change in anomalous SIE (that is, with respect to the mean for that calendar day), namely

$$\Delta E_i = \delta SIE_{i+1} - \delta SIE_i$$

where i denotes the day number and δ refers to anomalies. (Defining ΔE in this way eliminates the seasonal cycle and background conditions from the consideration of daily changes in SIE.) An analogous metric, ΔA, was defined for changes in ice *area*. ΔE and ΔA were calculated for every day in JJA between 1979 and 2016.

As a measure of winter subantarctic cyclone activity we identified all cyclones that occurred on each day in each sector. We then summed their 'depths' (represented as SD), and achieved a metric which represents the net vigour or influence of all cyclones on that day. We then found all zero-cyclone days and split SD into quartiles (from the least to most intense). Fig. 2 shows a clear upwards trend in ΔE and ΔA as summed cyclone depth increases in almost every sector. This means that, overall, more cyclone activity corresponds to increases in SIE and SIA on daily timescales. Further details of this research are presented in Thorn et al. (2019).

References

Dee, D. P. et al., 2011: The ERA-Interim reanalysis: Configuration and performance of the data assimilation system. *Quart. J. Roy. Meteor. Soc.*, **137**, 553-597.

Grieger, J. et al., 2018: Subantarctic cyclones identified by 14 tracking methods, and their role for moisture transports into the continent. *Tellus*, **70A**, 1454808.

Pezza, A. B., et al., 2012: Climate links and recent extremes in Antarctic sea ice, high-latitude cyclones, Southern Annular Mode and ENSO. *Climate Dyn.*, **38**, 57-73.

Simmonds, I., 2015: Comparing and contrasting the behaviour of Arctic and Antarctic sea ice over the 35-year period 1979-2013. *Ann. Glaciol.*, **56(69)**, 18-28.

Thorn, D. B. et al., 2019: The impact of regional storms on daily Antarctic sea ice variability. *Geophys. Res. Lett.*, (in review).

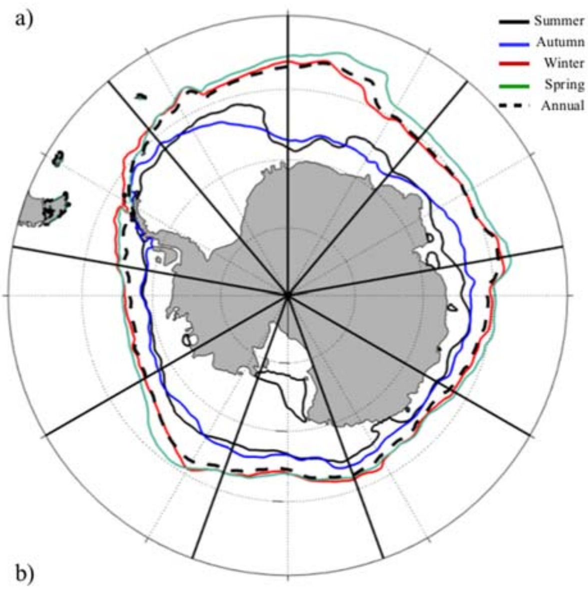

Fig. 1: Climatological sea ice edge for the seasons of summer (DJF), autumn (MAM), winter (JJA) and spring (SON) for 1979-2016. (Ice extents are from NSIDC NASA Team passive microwave data. These data were unavailable for December 1987-January 1988, so the DJF 1978-88 entry was computed by linearly interpolating anomalies from the adjacent months as in Simmonds (2015).)

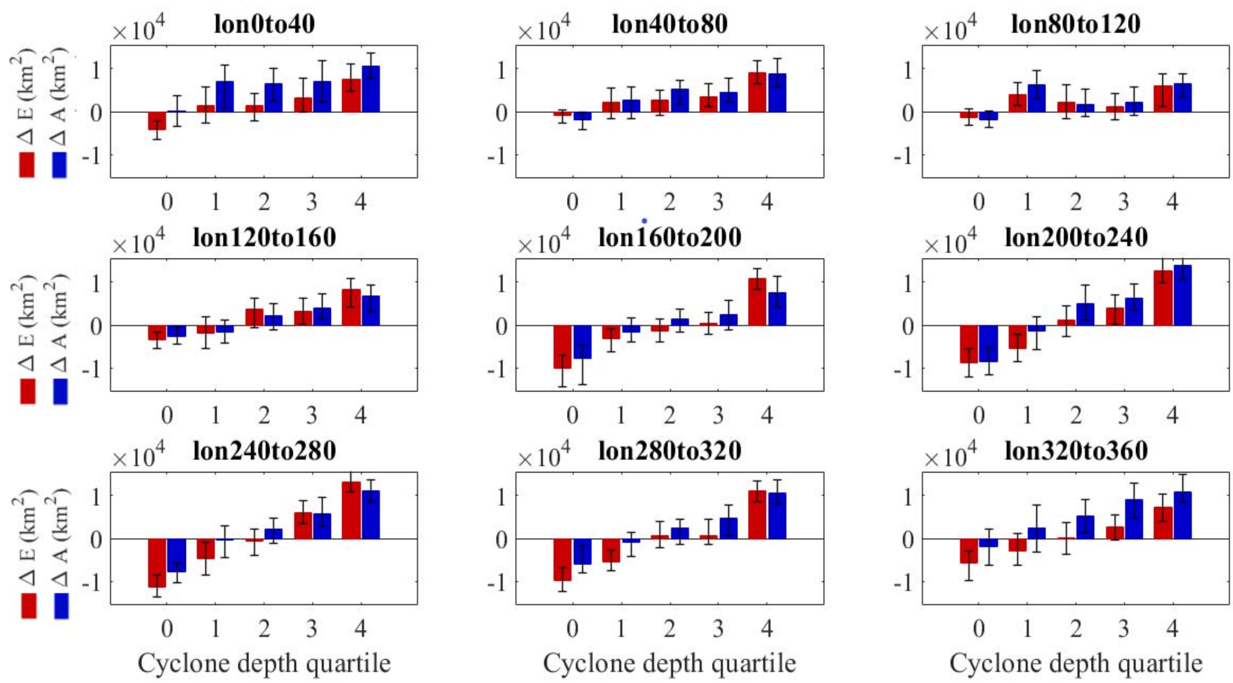

Fig. 2: Medians of ΔE (red) and ΔA (blue) in km^2 for each SD 'quartile'. Note that 'quartile zero' represents days with no cyclones. Whiskers represent the bootstrapped uncertainties (5-95th percentile)

Variations of precipitation-temperature relationship in spring-summer for Eurasian regions

Timazhev A.V.[1], Mokhov I.I.[1,2],

[1]A.M. Obukhov Institute of Atmospheric Physics RAS
[2]Lomonosov Moscow State University

timazhev@ifaran.ru, mokhov@ifaran.ru

According to observations since the end of 19th century there is a general decrease of precipitation in spring-summer months in mid-latitudinal European (AR) and Asian (AR) Russian regions under regional warming [1-5]. Figure 1 shows precipitation anomalies in May-July in dependence on corresponding anomalies of surface air temperature for ER and AR by data from [1,2] for the period 1891-2015. Here we estimate variations in the precipitation-temperature relationship in spring-summer months with the use of cross-wavelet analysis.

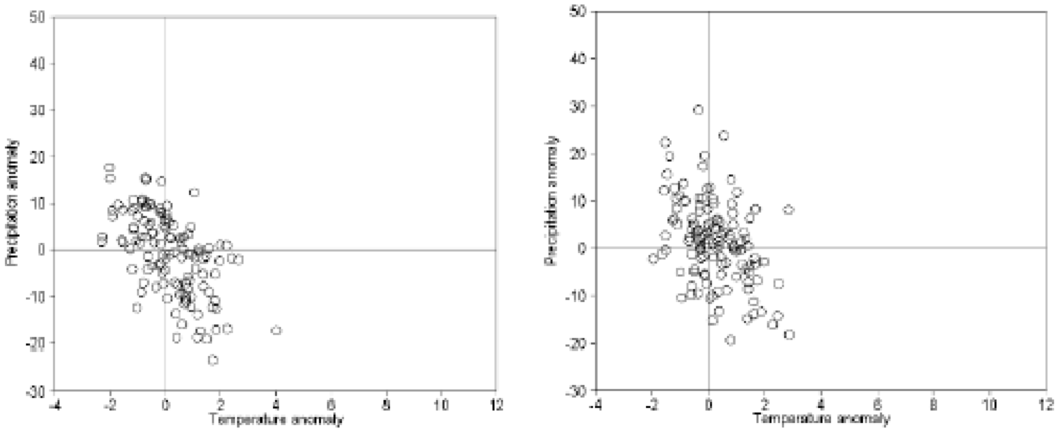

Fig. 1. Precipitation anomalies in May-July in dependence on corresponding anomalies of surface air temperature for ER (left) and AR (right) from observations for the period 1891-2015.

Figure 2 shows significant differences of local coherence of precipitation and surface air temperature in May-July for ER and AR from observations for the period 1891-2015. There is significant negative correlation between long-term variations of precipitation and temperature for ER. Such a correlation for AR is less significant, especially during last decades. On the other hand the negative correlation between precipitation and temperature for AR in May-July is remarkably more significant for interdecadal variations. Negative correlation between precipitation and temperature for interannual variations is displayed for some relatively short periods.

According to [5] climate model simulations with historical scenario display well-marked negative correlation between temperature and precipitation for ER and AR. Significant differences in the East Asian mid-latitudinal regions to the east from Baikal Lake (in the Amur River basin, in particular) can be related with the influence of the Asian monsoon. Under the warming scenarios in the 21st century, the range of precipitation fluctuations increases and the relationship between precipitation and temperature in midlatitudinal Eurasian regions becomes less significant as a whole [5].

In particular, according to model estimates the significant negative correlation between long-term variations of precipitation and temperature for ER can become insignificant to the middle of the 21 century or even earlier. In particular, according to model estimates, a significant negative correlation between precipitation and temperature in May-July in the European region may become insignificant by the middle of the 21st century or earlier.

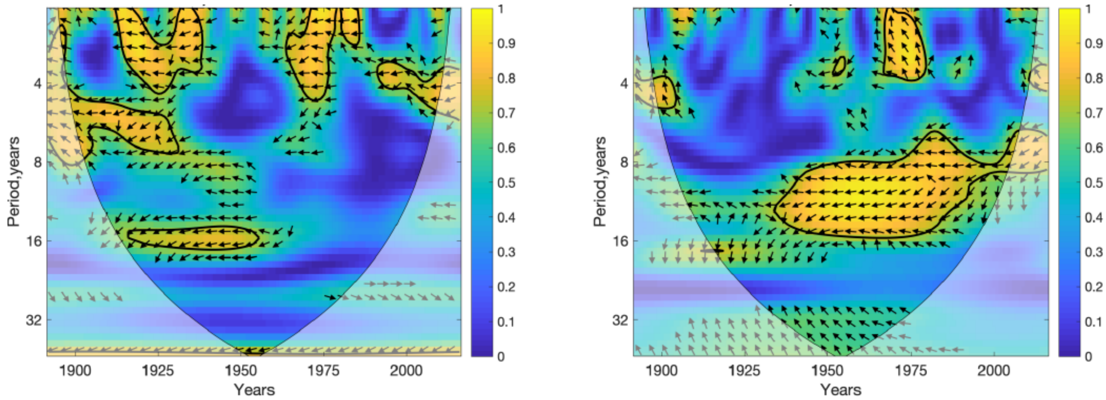

Fig. 2. Local coherence of precipitation and surface air temperature in May-July for ER (left) and AR (right) from observations for the period 1891-2015.

This work has been supported by the RSF (project No. 19-17-00240) using the results obtained in the framework of the RAS Presidium program "Climate change: causes, risks, consequences, problems of adaptation and regulation" and RFBR (projects No. 17-05-01097 and No. 17-29-05098).

References

1. Meshcherskaya A.V., Blazhevich V.G. The drought and excessive moisture indices in a historical perspective in the principal grain-producing regions of the Former Soviet Union. *J. Climate*, 1997, **10**, 2670–2682.
2. Mesherskaya A.V., Mirvis V.M., Golod M.P. The drought in 2010 against the background of multiannual changes in aridity in the major grain-producing regions of the European part of Russia. *Tr. MGO,* 2011, **563**, 94–121 (in Russian)
3. Mokhov I.I. Spring-summer climate extremes in Eurasian midlatitudinal regions. *Res. Activ. Atmos. Ocean. Modell.* J. Cote (ed.). Geneva: World Climate Research Programme. WMO TD-No.1276, 2005, 2.7-2.8.
4. Mokhov I.I., Dufresne J.-L., Khon V.C., Le Treut H., Tikhonov V.A. Regional regimes with drought and extreme wet conditions: Possible changes in XXI century from IPSL-CM2 simulations. *Res. Activ. Atmos. Ocean. Modell.*, WMO/TD-No. 1105, 2002, 07.31–07.32.
5. Mokhov I.I., Timazhev A.V. Precipition-temperature relationship in spring-summer for Eurasian regions: Model projections. *Res. Activ. Atmos. Ocean. Modell.* E. Astakhova (ed.). WCRP Rep. No 15/2018, 2018, S.7, P. 07-08.